The Nanocrystalline Coordination Polymer of AMT–Ag for an Effective Detection of Ciprofloxacin Hydrochloride in Pharmaceutical Formulation and Biological Fluid

4.1 Introduction

Nanocrystalline coordination polymers (NCCPs) are remarkably stunning for both scientific and technological applications as they explore significant innovations in creating advance materials with novel building blocks. The fascinating features of these valuable scaffolds originated because of their specific architecture, unique directionality, easy tunability, mesoporous morphologies, and high specific surface areas. Various advanced and emerging fields like catalysis, biological labeling, engineering of sensors, and solar energy harvesting are benefited by the rational scrutiny and tailoring of nanocrystalline coordination polymers. The faster electro kinetics and improved recyclability are the recently trending topics in the research on nanocrystalline coordination polymers. [Huanhuan et al., 2014; Nie et al., 2013; Oh et al., 2013; He et al., 2013; Malerba et al., 2015; Jin et al., 2012; Pham et al., 2011]. The engineering of individual nanocrystalline building blocks into controlled frameworks with diversified architectures for ameliorated functions have potential importance in materials science. The fine tuning of self–organization and π–π interactions of entity nanocrystalline materials, serve as a fascinating tool to offer promising and advanced nano and micro scaled structures to from diverse nano–objects [Hijikata et al., 2011; Bourzac, 2012; Gröschel, 2013; Martinez et al., 2010; Tanaka et al., 2010]. The designing and assembly of nanocrystalline building blocks with perfect accuracy, is an interdisciplinary field with numerous challenges, which requires enormous physical and chemical parameters to deal with. However, dearth of potential investigations is lack in this field and thus requires a special attention; a common and widespread blueprint covering the complete permutations, for the frontier applications in catalysis and sensing. It is advantageous and highly demanding to tune the promising features of nano–crystals with novel synthetic strategies in order to get highly insightful applications [Wu et al., 2009; Oh et al., 2005; Schreuder et al., 2008; Dipalo et al., 2015].

To sketch physical and chemical properties of targeted nanocrystalline building blocks according to their academic and industrial requirement is a noteworthy and valuable attentive point in this domain. Adequate original research reports are appearing in this area and those deliver nanocrystalline coordination polymers with fascinating and unique networks; and they certainly have pronounced ability for the construction of next generation redox material as well as intercalation electrodes. However, the critical assessment and wide spread scrutiny is required to widen the domain of these materials by unravel their unexplored features [Wright, 2014; Wang et al., 2005]. Redox active NCCPs with adequate surface area are significantly stunning for electrochemical applications because of their greater power density aspects with appropriately maintained energy density. Efficient efforts and approaches have been especially dedicated to shorten and control the crystal size of coordination polymers up to nano–scale. Reduction in crystal size results a dramatic decrease in diffusion pathway and thus leading to epilogue that size dependent diffusion coefficient, plays a critical role in the permeability of roomer. Moreover, ligand plays a creative function and acts as a critical building block in the draft sketching of NCCPs [Cheng, 2007; Baumberg, 2009; Tanaka et al., 2010; Zhang et al., 2011]. In this context, 2–amino–5–mercapto–1,3,4–thiadiazole (AMT) is an efficient architecture–directing organic linker used in the fabrication of functionally tailored NCCPs as the sulfydryl sulfur and two nitrogen atoms facilitates the metal linkage with the ligand in an infinite array, which is also advantageous for several electrode modifications and sensing applications. Moreover, the π–π stacking and hydrogen bonds direct towards a definite orientation and arrangement of these building blocks. Metal–ligand interactions are proficiently more pronounced than other existing non–covalent interactions causing more robust entities. Furthermore, the metal incorporation in NCCPs expands the range of functional properties and allows fashioning the strategies based on metal–addressed assembly [Haedler et al., 2015]. In the perspective of all the above facts, and as a part of our ongoing research interests in the synthesis of novel nanoporous coordination polymers using affordable building blocks, we are first time exploring the synthesis, characterization and nano–sensing properties of a nanocrystalline coordination polymer (NCCP) comprising AMT–Ag network. The synthesis of AMT–Ag NCCP was accomplished at ambient temperature under optimal conditions without any additional additives (Figure 4.1). In this synthesis, the reactant concentration was customized and optimized with the reaction progress; it is thoroughly probed by various characterizing tools. The Ag(I) ions assist the coordination to the ligand having unsaturated nitrogen and sulphur atoms thus providing an architecture with coordination number two to six [Lee et al., 2010].

Now–a–days there are several lifesaving drugs commonly used in daily life, and they have a toxic effect when their dose exceeds over a certain limits. Ciprofloxacin is a broad spectrum fluoroquinolone antibiotic, extensively used in the treatment of both gram positive and gram negative bacteria, including a number of severe infections such as, respiratory tract infections, typhoid fever, anthrax, urinary tract infections, malignant otitis externa and chancroid [Lubick, 2011; Montes et al., 2014; Zhang et al., 2014]. Further, the overdose causes severe hepatotoxicity; therefore it is mandatory to screen CFX in human urine to track drug accumulation in hepatic patients to diagnose the CFX poisoning. CFX analysis is also important in drug quality control [Zhang et al., 2013; Garbellini et al., 2015; Wang et al., 2014]. Therefore, it is necessary to establish an easy going, quick, highly sensitive and reliable approach to assay CFX in clinical formulation and biological fluids. The existing techniques used for the detection of CFX, high performance liquid chromatography (HPLC) [Vybiralova et al., 2005], spectro–fluorimetry [Billah et al., 2014], spectrophotometry [Wang et al., 2011] are limited due to high cost, tedious procedure, requirement of sophisticated instrumentation, a narrow range in the limit of detection, and the problems associated with their practical utility. The prepared AMT–Ag, NCCP is successfully employed in the voltammetric detection of CFX. Further the effective utility of the concept is proved by employing the detection of CFX in pharmaceutical assay and biological fluid. The present detection method is simple, portable and a cost effective electrochemical technique circumventing the drawbacks of existing methods.

4.2 Experimental

4.2.1 Materials

The AMT was obtained from Sigma–Aldrich chemicals, USA. Ciprofloxacin hydrochloride, ethanol, silver nitrate, borax, sodium hydroxide, BHT and TEMPO were procured from SRL chemicals, India and were utilized as received unless otherwise mentioned and ciprofloxacin hydrochloride sample solution was freshly primed and diluted using doubly deionized water. The electrode utilized for the construction of carbon paste electrode was obtained from Bio–analytical Systems. Human urine samples were collected from a non–smoking volunteer (male, 32 y, 76 kg and 171 cm). All urine samples and eye drops were prepared and investigated on the same day of collection.

4.2.2 Electrode fabrication

The carbon paste electrode (CPE) body of 1 mm diameter utilized for the modification was acquired from BASi, Indiana. The well of the electrode was filled with an active paste of graphite powder (67% w/w), nujol oil (2.5% w/w) and AMT–Ag (30% w/w). Then CPE was made flat on a butter paper in order to get smooth surface. Similarly the unmodified CPE was also constructed.

4.2.3 Instrumentation

The FT–IR spectra were executed on KBr disc in the region 3500–400 cm^{-1} and recorded with Nicolet–6700, USA, FT–IR spectrometer. The Perkin Elmer Lambda–25 spectrophotometer was used to record UV–Vis by using a quartz cuvette (optical path length 1 cm). TGA was performed on TGA/DSC 1 STARE System, Switzerland (temperature ramp of 20 °C min^{-1} under N_2). The powder X–ray diffraction pattern for the AMT–Ag and AMT was carried out by a rotating anode X–ray diffractometer (18 kW, Cu–Kα radiation, graphite monochromator, 3°/min scan rate, Rigaku, Japan) from 10° to 80°. The elemental analysis was carried out with X–ray photoelectron spectrometer, Kratos Analytical Instrument, Shimadzu, Amicus XPS, UK. The FE–SEM and Energy–dispersive X–ray were conducted on Curl Zeiss, Supra–40, Germany. The voltammetric experiments were conducted on Computrace ion analyzer, Switzerland (Ω Metrohm, 797 VA) by electrochemical software 3.1 using three electrode assembly with AMT–Ag modified CPE (working electrode), Pt foil (counter electrode), and Ag/AgCl (reference electrode) for all electrochemical measurements using phosphate buffer (pH = 7.0) (supporting electrolyte).

4.2.4 Typical Experimental Procedure for AMT–Ag Synthesis

In the typical synthesis of AMT–Ag, a solution of AMT in EtOH (30 mM) was added drop wise to an ethanolic solution of $AgNO_3$ (100 mM) in a R. B. flask and the constituents were stirred vigorously for 18 h in open atmosphere. A white AMT–Ag nanocrystalline coordination polymer was precipitated. The precipitate thus formed was then filtered and washed several times (5 mL x 5) with water–ethanol (2:1) mixture in order to remove the unreacted $AgNO_3$ and AMT. After drying the yield obtained was 81%.

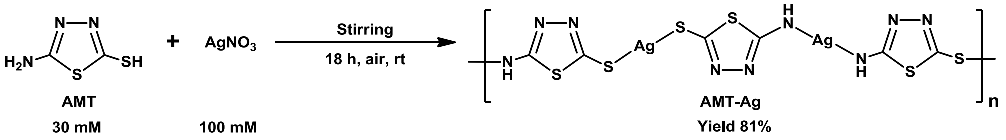

Figure 4.1 The synthesis of AMT–Ag.

4.3 Results and Discussion

Herein, AMT–Ag is an immensely symmetrical molecule that reinforces the radial coordination–bonding sites to form a well–established network based on the multiple cooperative interactions with the unique ability to form π–π stacking through the aromatic array of network.

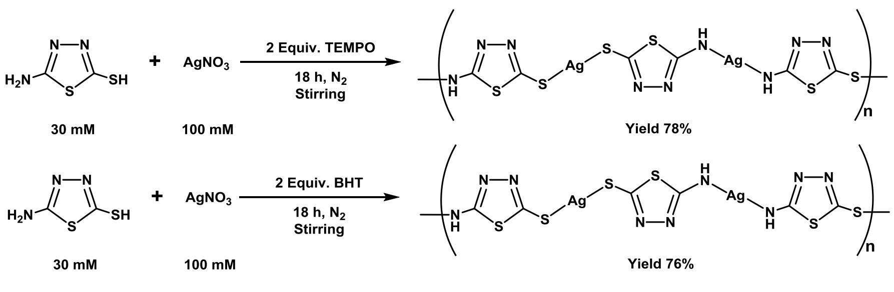

Figure 4.2 Controlled experiments for the formation of AMT–Ag using TEMPO and BHT.

The reaction mechanism for the formation of AMT–Ag is enlightened in the view of radical controlled experiments with trapping agents like (2,2,6,6–tetramethyl–1–piperidinyl)oxidanyl (TEMPO) and 2,6–di–*t*–butyl–4–hydroxytoluene (BHT) (Figure 4.2), that did not interfere with the reaction outcome under standard conditions concluding a plausible involvement of a cationic pathway (Figure 4.3).

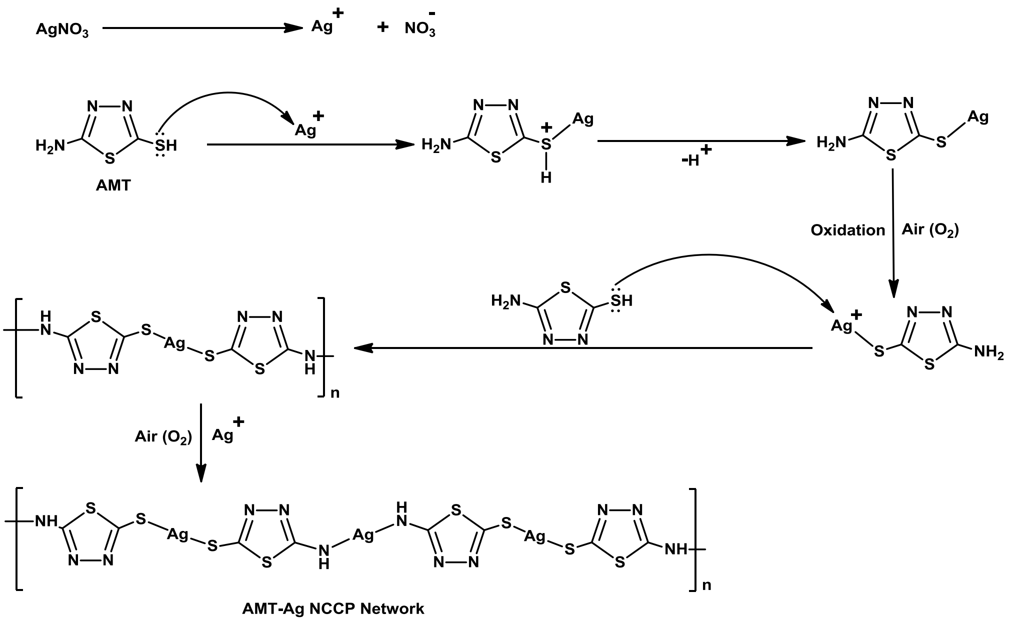

Figure 4.3 A Plausible mechanism for AMT–Ag formation.

Here, the $AgNO_3$ itself act as a cationic coordinating partner and start the polymerization reaction with AMT and forms metal incorporated monomer units in the presence of air (O_2), which triggers the Ag oxidation and serves a necessary helping hand and progress the reaction to deliver AMT–Ag, NCCP network [Shi et al., 2012; Allam et al., 2011; Allam et al., 2015; Singh et al., 2015]. The bonding interaction of AMT–Ag is thoroughly investigated through FT–IR and XPS. The FT–IR spectrum of AMT displayed several peaks appear in the region 3000–2700 cm^{-1}, and are assigned to

C–H stretching, Fermi resonances, and overtones (Figure 4.4). The vibrational frequency in the range 3160–3350 cm^{-1} is originated by υ(N–H) in AMT and significantly attenuated towards 3170–3300 cm^{-1} in AMT–Ag, emphasizing the linkage of exocyclic N–H with silver, since it is more basic than the endocyclic N–H bond. Further, the S–H stretching appears at 2760 cm^{-1} in AMT, and gets vanished in AMT–Ag; which confirms the ionization of the thiol group and bonding through the silver atoms. More evidently, the thioamide band I 1560 cm^{-1} in AMT shift appreciably toward higher wave number 1604 cm^{-1} in AMT–Ag resulted from a drop in the frequency of major contribution partner δ(N–H), and a significant rise in the frequency of minor contribution partner υ(C=N) respectively; caused by the bonding of silver with sulphur. Additionally, the characteristic thioamide band II 1340–1370 cm^{-1} in AMT which have major frequency contribution from υ(C=N) raised significantly to 1390 cm^{-1} in AMT–Ag, and thus support the bonding of silver with sulphur. Further, the X–ray photoelectron spectroscopy (XPS) of AMT–Ag is recorded at room temperature in order to investigate the oxidation state of Ag centers and chemical environment of the atoms present. The peaks are fitted using XPS peak 4.1 software (Figure 4.5). The Ag(3d) is best fitted with two doublets. The major contribution of binding energy at 372.2 eV is the characteristic of $3d_{3/2}$ Ag(I) [Fan et al., 2014]. However the binding energy at 366.0 eV corresponds to the $3d_{5/2}$ of Ag(I) approving the metal oxidation state in the polymeric skeleton. The deconvolution of S(2p) peak provides two sets of doublets arising from spin–orbit interaction. The aromatic sulphur atom exhibits binding energy values approximately 162.2 eV and 164.7 eV corresponding to S ($2p_{3/2}$) and S ($2p_{1/2}$). The exocyclic sulphur atom attached to the silver atom yield two fragments, laying at 163.5 eV and 167.6 eV for S ($2p_{3/2}$) and S($2p_{1/2}$) peaks respectively. A shifting in binding energy signifies the coordination of silver atom with exocyclic sulphur atoms. The peaks of N(1s) are best en suited with a pair of segments; the binding energy at 400.5 eV is the characteristic of endocyclic imine nitrogen (=N–). The inferior energy at 399.7 eV credited to the –NH groups, which further approves the attachment of nitrogen of –NH with silver to result an energy shift towards an elevated binding energy. The C(1s) spectrum with binding energy 287.5 eV and 289.5 eV present the appropriate fit corresponding to –N=C–S– and –N=C–N– bonding respectively [Lv et al., 2014]. Further, after a careful evolution of the pattern of X–ray diffraction a detailed structural confirmation of AMT–Ag was established. The X–ray diffraction pattern of AMT–Ag is stacked with AMT and Ag(0) confiscated from JCPDS file (CAS number 89–3722) (Figure 4.6a). Interestingly, there is no evidence of reduction of Ag(I) in NCCP, AMT–Ag, further the signature of AMT diffraction is not appearing in AMT–Ag. Figure 4.6b reveals the observed XRD pattern as dots, calculated pattern as a continuous line, and the difference as continuous bottom line for AMT–Ag achieved following Le–Bail fit of the XRD data using space group "monoclinic Pm". The Bragg peak locations in the difference plot are indicated as vertical tick marks. An auto–indexing program DICVOL04.51 is initially used to index X–ray diffraction of AMT–Ag [Young, 1996; Carvajal, 1993]. It was possible to index the experimental diffraction peaks using orthorhombic and monoclinic cells. Further, for the structural confirmation, the full pattern profile matching analysis was conducted using Le–Bail refinement with the help of FullProf [Boultif et al., 1991]. The XRD pattern of AMT–Ag, NCCP has been analyzed by Le–Bail refinement with several possible crystal structures orthorhombic Pnma, monoclinic P21/m and Pm space groups. The best refinement with the good figure of merit is obtained for monoclinic architecture that indexed all the diffraction peaks for AMT–Ag. The solution with the highest symmetry in monoclinic structure with Pm space group is accepted as the monoclinic cell is found a = 25.064(1), b = 6.5915(1), c = 8.6976 (2), β = 92.79(4), with no other observable systematic extinctions. The direct unit cell volume is 1435.26(1) Å^3.

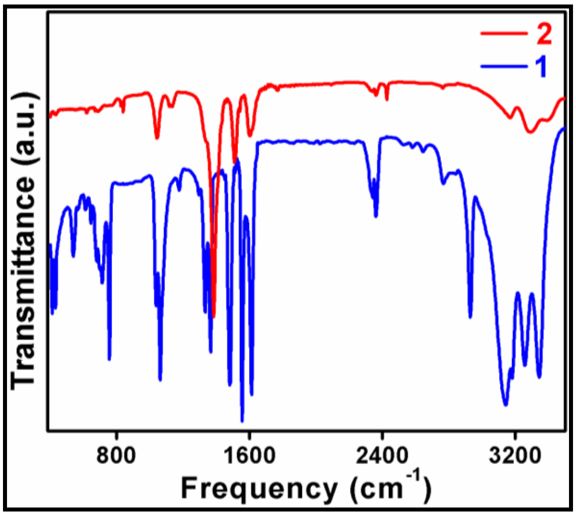

Figure 4.4 FT–IR spectra of AMT (1) and AMT–Ag (2).

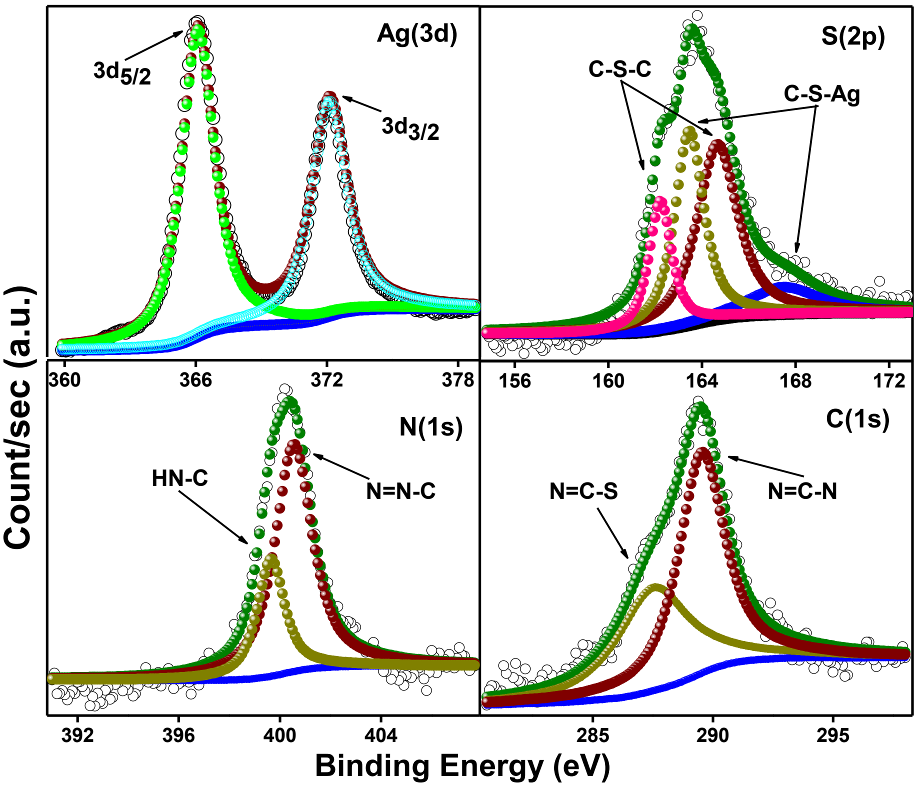

Figure 4.5 XPS spectra of AMT–Ag for Ag(3d), S(2p), N(1s) and C(1s) regions.

The particle size for nano–crystallites were calculated from the Rietveld method, using input files with the instrumental resolution function, obtained using silicon as a standard. Here, Thomson, Cox and Hasting approximation is performed to sort out the micro–structural effects in FullProf, and thus the average particle size is calculated as ~58(2) nm. [Shankar et al., 2015]. The result, further accounting the particle size through various peaks is in consistent with that evaluated ~61 nm using Scherrer formula [Reddy et al., 2016] and also visible in FE–SEM micrograph. The field–emission scanning electron microscopy investigation (Figure 4.7) reveals grasped nano–sized granules of AMT–Ag. Moreover, the elemental confirmation of AMT–Ag network corresponding to FE–SEM micrograph ensures the presence of elements carbon, nitrogen, sulphur and silver (Figure 4.8). Furthermore, the molecular modeling is executed in order to acquire the preferred orientation of ligand in the polymeric array (Figure 4.9) which establishes the anti–alignment as the preferred orientation.

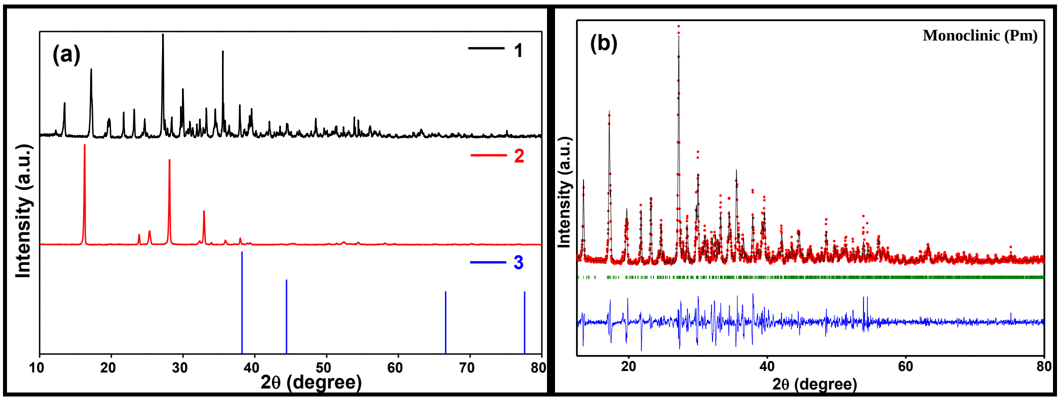

Figure 4.6 (a) XRD of AMT (1), AMT–Ag (2) and Ag(0), taken from JCPDS file CAS number 89–3722 (3); and (b) Le–Bail fit of AMT–Ag.

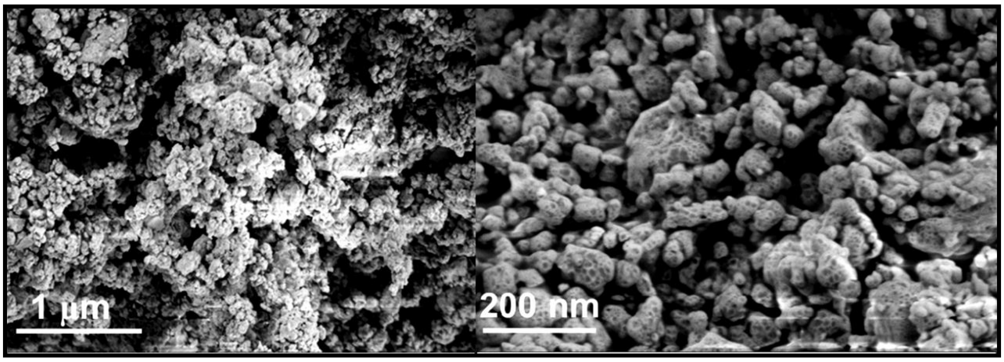

Figure 4.7 Field–Emission SEM micrograph of AMT–Ag.

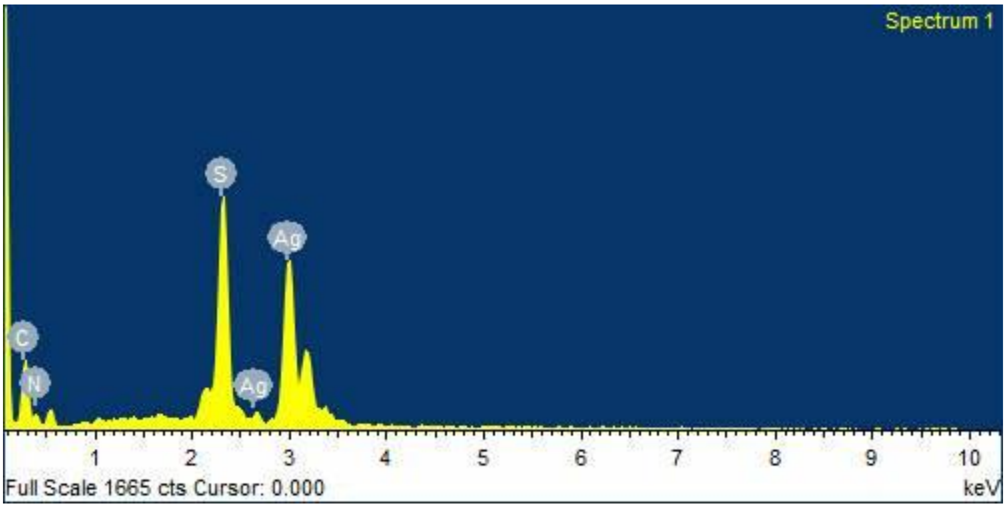

Figure 4.8 EDX of AMT–Ag provided by FE–SEM micrograph.

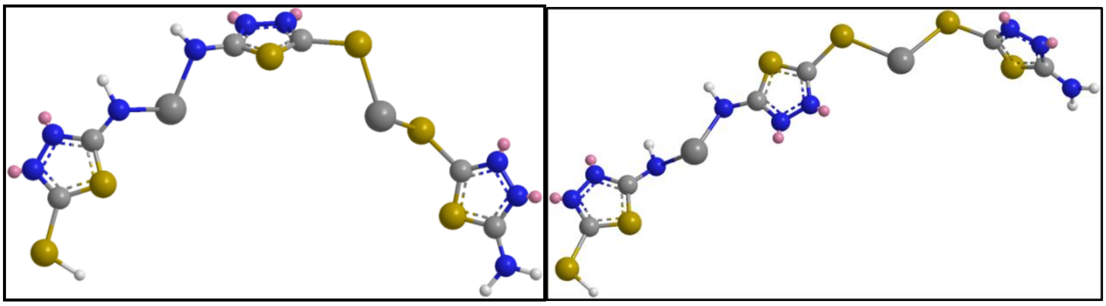

Figure 4.9 Ball–stick model structure of AMT–Ag in the *syn* (left) and *anti* (right) alignment generated by CS 3D Chem BioDraw Ultra 12.0 with structural energetic minimization. Here blue, cyan, light grey, golden, dark grey (large size) and pink balls represent N, H, C, S, Ag atoms and lone pairs.

Table 4.1 Interaction parameters involved in three AMT–Ag molecular fusions.

Energy (kcal/mol)	*Syn*–alignment (1)	*Anti*–alignment (2)
Stretch	0.4782	0.4323
Bend	14.1238	13.2258
Stretch–Bend	–0.2935	–0.2229
Torsion	1.5535	0.7687
Non 1,4–VDW	–2.5690	–2.2030
1,4–VDW	5.2435	4.1514
Charge–charge	–	–
Charge–dipole	–	–
Dipole–dipole	–5.0931	–5.9030
Total energy	13.4435	10.2493

These calculations are executed by considering dipole–dipole interactions along with other existing interactions by varying the orientation of polymeric chain (*cf.* Table 4.1). It is clear from the table that total energy is least for the *anti*–alignment rather than *syn*–alignment; the entirely responsible phenomenon for overall increased energy resulted from misalignment of orbital coplanarity. Based on the results anticipated, the structural network of AMT–Ag is proposed (Figure 4.10) which supports the outcomes. The Ag(I) centers are linked with AMT by exocyclic sulphur and nitrogen atoms throughout the array and the adjacent layers are stabilized *via* π–π stacking of aromatic rings and intermolecular hydrogen bonding. Further, the electronic absorptions of AMT–Ag are examined through UV–Vis spectroscopy. AMT exhibits n–π* and π–π* transitions transition at 317 nm and 202 nm respectively (Figure 4.11) and a bathochromic shift in NCCP, AMT–Ag displaying n–π* and π–π* transitions at 341 nm and 207 nm are attributed due to the interaction of AMT with Ag(I) [Hua et al., 2015]. Additionally, the thermal stability and activation energy for thermal decomposition of NCCP are scrutinized by thermo–gravimetric analysis. TGA curve of AMT–Ag, measured under nitrogen atmosphere (Figure 4.12), reveals a dramatic weight loss divulging the thermal stability up to 160 °C providing the thermally robust extended scaffold network.

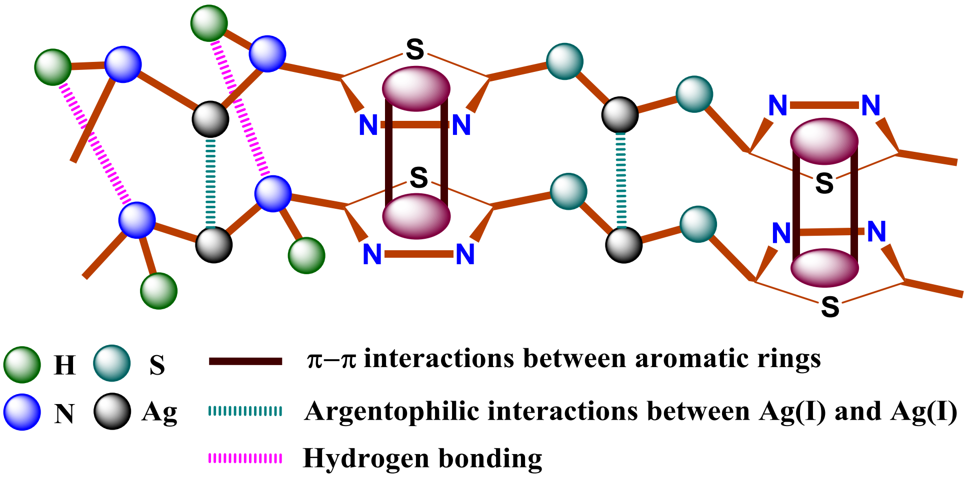

Figure 4.10 Proposed structural network of AMT–Ag.

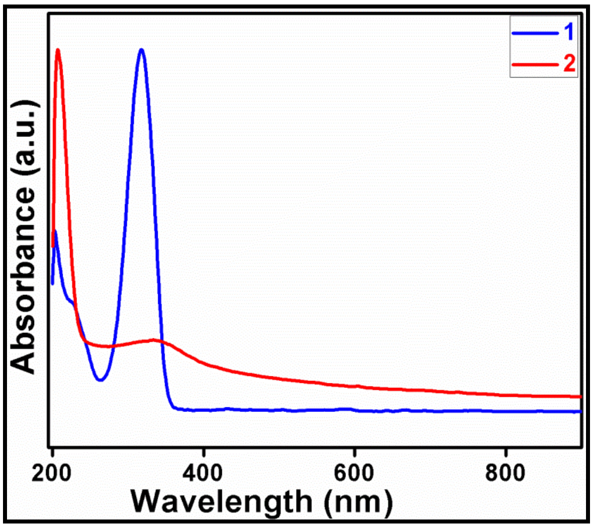

Figure 4.11 UV–Vis of AMT (1) and AMT–Ag (2).

Moreover, the minor degradation up to 3% in the temperature range of 100 °C is due to non–coordinated water molecules adsorbed to the lattice of AMT–Ag and the first decomposition at 160 °C is due to cleavage of coordination linkage of metal and ligand. Further, the successive degradation is caused by thermal disintegration of byproducts.

In the DTA plot of AMT–Ag, it manifests an exothermic peak corresponding to the TGA plot. The activation energy corresponding to thermal degradation is evaluated by using Briodo equation [Tiwari et al., 2014]. The slope of the plot (Figure 4.13) provides the activation energy for the thermal decomposition of AMT–Ag 21.1 kJ/mol.

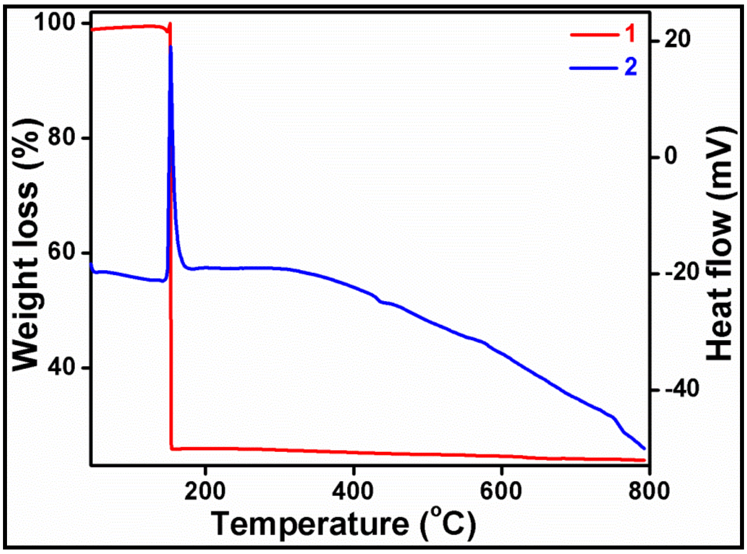

Figure 4.12 TGA (1) and corresponding DTA (2) plot of AMT–Ag.

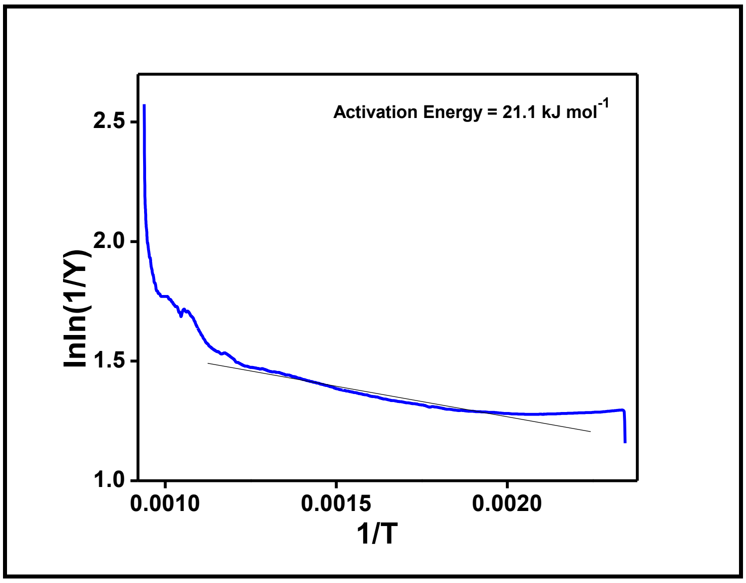

Figure 4.13 Thermal activation energy plot of AMT–Ag.

4.3.1 Electroactivity of AMT–Ag

Initially the electro activity of AMT–Ag modified CPE (AMT–Ag/CPE) is thoroughly probed *via* CV using Fe(II) /Fe(III) redox system (0.01 M) in 0.1 M PBS pH 7 at a fixed scan rate of 50 mV/sec (Figure 4.14). The AMT–Ag/CPE reveals the quasi–reversible redox peaks increased by a factor of 7 to the unmodified CPE, caused by the (i) robust electron channeling through the nanocrystalline pores of AMT–Ag, (ii) the electrostatic interaction between Fe(II) /Fe(III) redox couple and nitrogen, sulphur atoms, and (iii) the increased electro–active surface area. The perusal of outcome attributed that AMT–Ag is an excellent redox mediator for electrochemical sensing, providing the facile accessibility of nanopores through interconnection of the diverse dimensions.

4.3.2 Calculation of Active Surface Area of Electrode

The surface properties of AMT–Ag modified electrode is investigated using Fe(II) /Fe(III) redox couple as a probe and the active surface area of AMT–Ag/CPE, unmodified CPE are evaluated in accordance with Randles–Sevcik equation (Equation (4.1).

$$i_p = 2.69 \times 10^5 n^{3/2} A D^{3/2} C \upsilon^{1/2} \quad \cdots\cdots\cdots\cdots (4.1)$$

Here D is diffusion constant of Fe(II) /Fe(III) redox couple (7.6×10^{-6} cm^2 s^{-1}), C represents the concentration of Fe(III), n stands for number of electron engaged in electro–oxidation and A belongs to the active surface area of unmodified CPE and AMT–Ag/CPE, evaluated as 0.03 cm^2 and 0.14 cm^2 respectively.

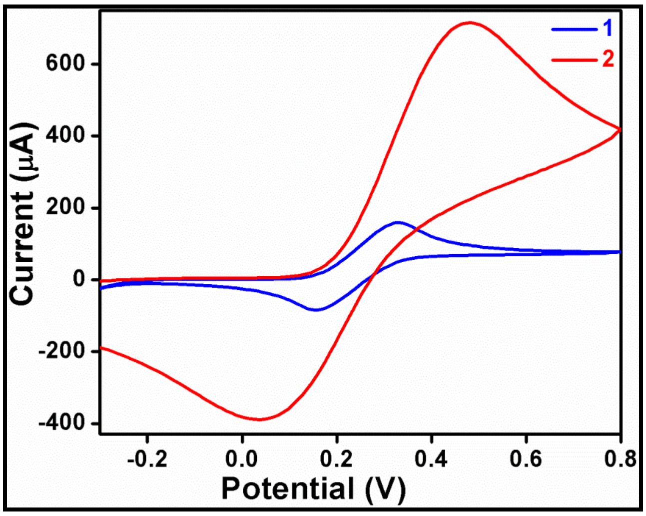

Figure 4.14 CV of the electrodes in 0.01M Fe(II) /Fe(III) in PBS pH 7 unmodified CPE (1) and AMT–Ag/CPE (2) scans *vs* Ag/AgCl at 50 mVs^{-1}.

4.3.3 Evaluation of Number of Electron Transferred

The number of electrons involved in electro–oxidation of ciprofloxacin at AMT–Ag modified electrode can be scrutinized by the shifting in anodic peak potential with scan rate (Figure 4.15a). The irreversible anodic peak potential increases linearly with log υ as depicted in (Figure 4.15b).

Further the regression equation (Equation 4.2) followed by the irreversible anodic peak is

$$E_p = (0.906 \pm 0.013) + (0.033 \pm 0.002) \log \upsilon \cdots\cdots\cdots\cdots\text{(4.2) With } R^2 = 0.987.$$

$$E_p = E^\circ + (RT/\alpha n_a F)\ln\left(\frac{RT k_f^\circ}{\alpha n_a F}\right) - \left(\frac{RT}{\alpha n_a F}\right)\ln \upsilon \cdots\cdots\cdots\cdots\cdots\cdots\text{(4.3)}$$

Correlating the above with Laviron equation (Equation 4.3) [Laviron, 1974]. Here n_a represents the number of electrons transferred during electro–oxidation, α stands for transfer coefficient, R for gas constant, k_f° belongs to the standard heterogeneous rate constant, E_p for anodic peak potential. The value of n_a computed as 1.56 ensuring that irreversible electro–oxidation of ciprofloxacin is a two electron process at AMT–Ag/CPE platform, which is in agreement with the literature [Osman et al., 2015]. A graph between anodic peak current (i_p) against square root of scan rate ($\upsilon^{1/2}$) is plotted (Figure 4.15c) to classify the nature of electrochemical oxidation; whether the process at the AMT–Ag/CPE is diffusion or adsorption controlled. The linear relationship with the regression value 0.997 suggest that electro–oxidation of CFX at AMT–Ag/CPE is a diffusion controlled process with a linear equation (Equation 4.4).

$$i_p = (0.71 \pm 0.02)\upsilon^{1/2} - (0.23 \pm 0.0.01)\cdots\cdots\cdots\cdots\cdots(4.4)$$

Additionally here the non–zero value of ordinate intercept depicts the associated adsorption at the surface of electrode [Osman et al., 2015].

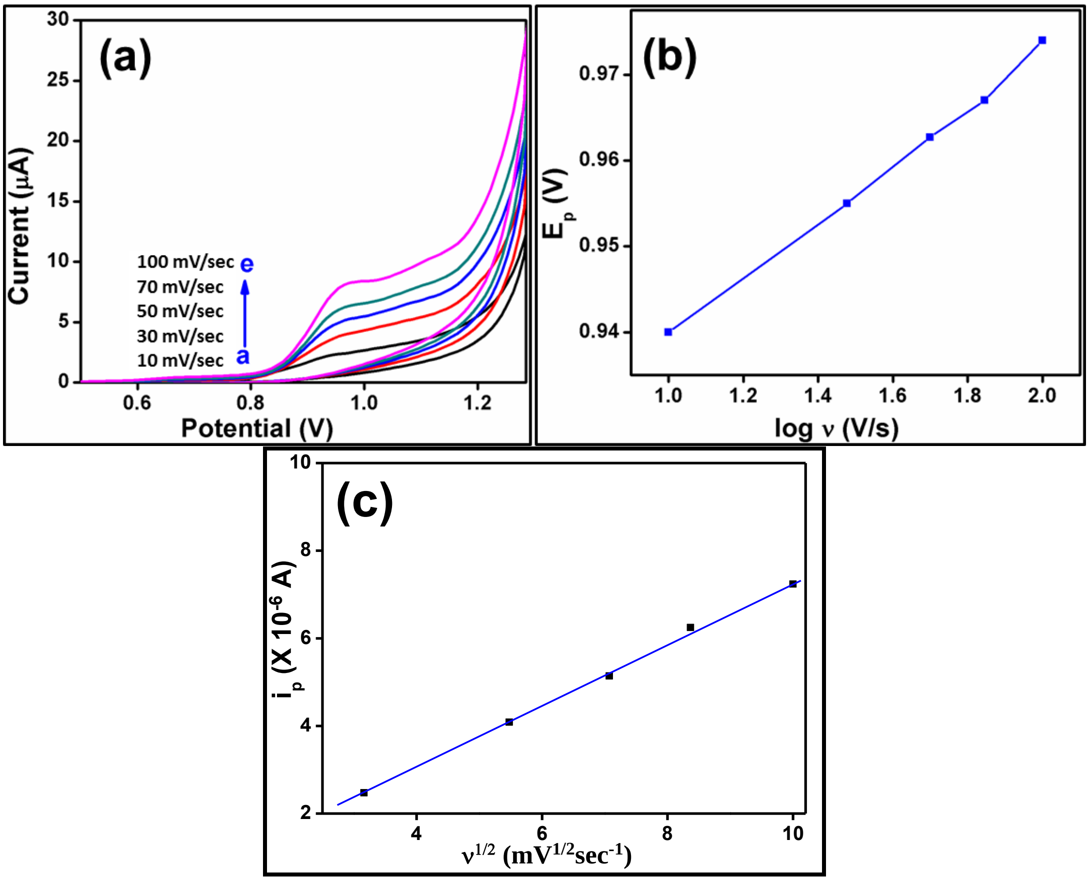

Figure 4.15 (a) CV of AMT–Ag/CPE in 18 μM CFX at scan rates 10, 30, 50, 70 and 100 mV, (b) plots of the CFX anodic peak potentials against log υ and (c) anodic peak current against $\upsilon^{1/2}$.

4.3.4 Electrochemical detection of CFX

To disclose the sensitivity and electro–analytical application of the AMT–Ag, a thorough investigation has been probed using AMT–Ag/CPE for the electrochemical oxidation of fluoroquinolone antibiotic, CFX in PBS pH 7. The characteristic anodic peak at +1.0 V in DPV (Figure 4.16a) and CV (inset) using AMT–Ag/CPE platform signifies the electro–oxidation of CFX.

The detailed experimentation is conducted to establish the assignments of each addition of drug in signature events, and to assure the thorough mixing of solution, electrode was rotated at 600 rpm for 10 min. Additions of CFX results an enhancement in the anodic current with a tiny potential displacement in anodic regions, strongly endorsing the effect of CFX concentration to the signature anodic domain. A linear calibration curve is obtained for total five consecutive experiments within a series of 18 µM to 180 µM. The calibration plot provides the limit of detection 5 nm with sensitivity 0.001 µA/µM at signal–to–noise ratio (S/N) 3 (Figure 4.16b).

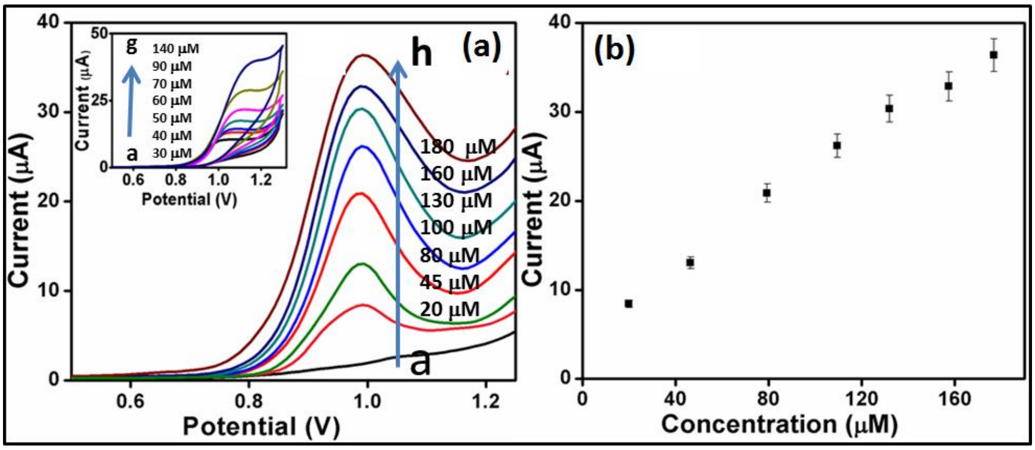

Figure 4.16 DPV response by the serial addition of CFX to AMT–Ag/CPE in PBS pH 7, (b) corresponding calibration plot. Inset shows the CV response by serial addition (scans *vs* Ag/AgCl at 50 mVs^{-1}).

The outcome of the results is a consequence of the following reasons: (1) the π–electrons of AMT–Ag are capable of interacting with CFX via π–π electron coupling, promoting the rapid electron transfer; (2) AMT–Ag possessed a large number of nitrogen and sulphur atoms that provide electrostatic anchoring points for CFX; (3) the hydrophobic interactions and formation of hydrogen bonds between AMT–Ag and CFX (4) the high electro–catalytic proficiency of Ag facilitates the easier path to electro–oxidation of CFX. Based on these consequences, AMT–Ag/CPE efficiently delivers an enhanced current response. The detection strategy of the present voltammetric sensing is displayed schematically (Figure 4.17). In the electro–oxidation of CFX, the N–H group gets oxidized into N–OH through zwitterion intermediates [Laviron, 1974].

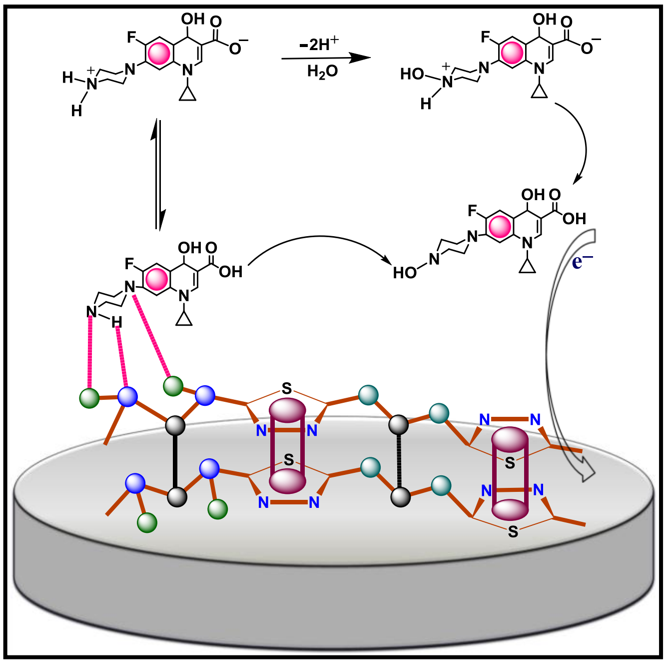

Figure 4.17 Proposed schematic illustration for the electro–oxidation of CFX at AMT–Ag/CPE.

4.3.5 Application of CFX Detection Method in Pharmaceutical Formulation

CFX is a broad spectrum antibiotic and active pharmaceutical ingredient having tremendous implications to human life. So, in order to correlate and cross–check the results obtained by the AMT–Ag/CPE assisted electrochemical oxidation of CFX and to examine the versatility of the sensing strategy, the strategy employed for the CFX in a clinical formulation i.e. eye drop, buffered to the optimized pH of 7. The voltammetric response of clinical formulation is explored using the same experimental parameters as used under ideal conditions and depicted in figure 4.18. The addition of CFX resulted to a clear anodic peak at +1.0 V (*vs* SCE) and manifest a remarkable spiked anodic peak current with the successive addition of the eye drop sample as scrutinized by DPV and CV (inset) voltammogram (Figure 4.18a) evidencing proof of concept been established in clinical formulation. Based on the calibration plot corresponding to DPV (Figure 4.18b), the detection limit and sensitivity is estimated as 22 nM and 0.002 μA/μM respectively (S/N 3); suggesting the potential applicability of the proposed strategy for the ultra–trace assay of CFX. Furthermore this electrochemical approach is employed in human urine received from healthy and adult volunteer in order to observe any potential practical complications that might be associated when screened real samples. The human urine is collected and a sample is prepared using 0.1 M PBS (20: 80; urine: 0.1 M PBS; pH 7). The spiked characteristic CV signature is observed in human urine (inset) for CFX indicating the specific nature of the methodology and ruled out the possible intrusion from other constituents in biological fluids. The electrochemical procedure is repeated in DPV, with a sample of human urine (Figure 4.19 a) and the sensitivity of the CV signature in a true urine matrix is précised using a calibration plot (Figure 4.19b). Therefore, these results are crystal clear in demonstrating the success of this newly engineered electrode material that facilitates the voltammetric assay of CFX in human urine displaying a detection limit and sensitivity as 60 nM and 0.007 μA/μM respectively at signal–to–noise ratio (S/N) 3 and is shown to be valid in biological fluid without any interference. Further a comparative study to CFX detection through several reported methods and the proposed approach are related through a bar diagram (Figure 4.20). It is presenting a surrogate for the effectiveness of sensor and furnishing the epilogue that the proposed strategy executes the least detection limit among the other methods for CFX detection.

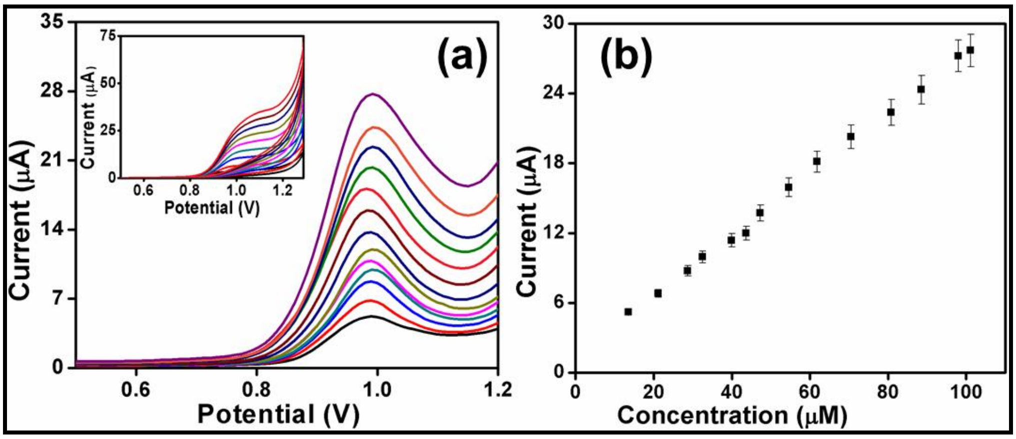

Figure 4.18 (a) DPV response by the serial addition of eye drop at AMT–Ag/CPE in PBS pH 7, (b) corresponding calibration plot. Inset shows the CV response by successive additions (scans *vs* Ag/AgCl at 50 mVs^{-1}).

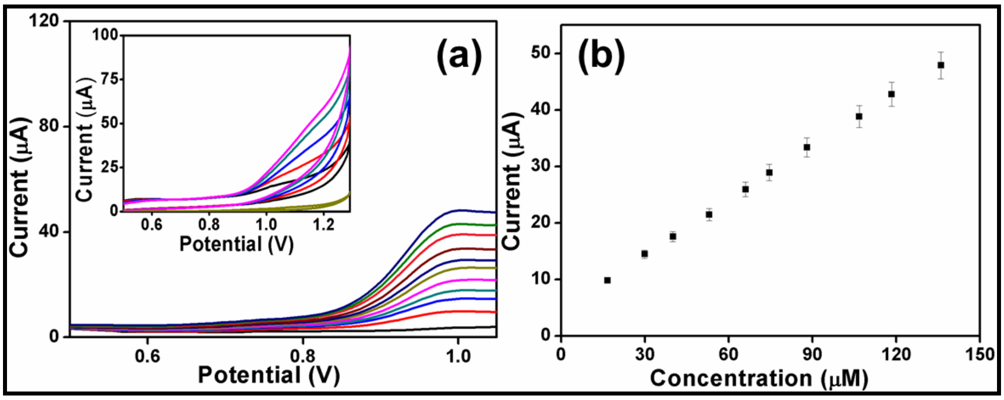

Figure 4.19 (a) DPV response by the serial addition of CFX in biological fluid at AMT–Ag/CPE in PBS pH 7, (b) corresponding calibration plot. Inset shows the CV response by successive additions (scans *vs* Ag/AgCl at 50 mVs^{-1}).

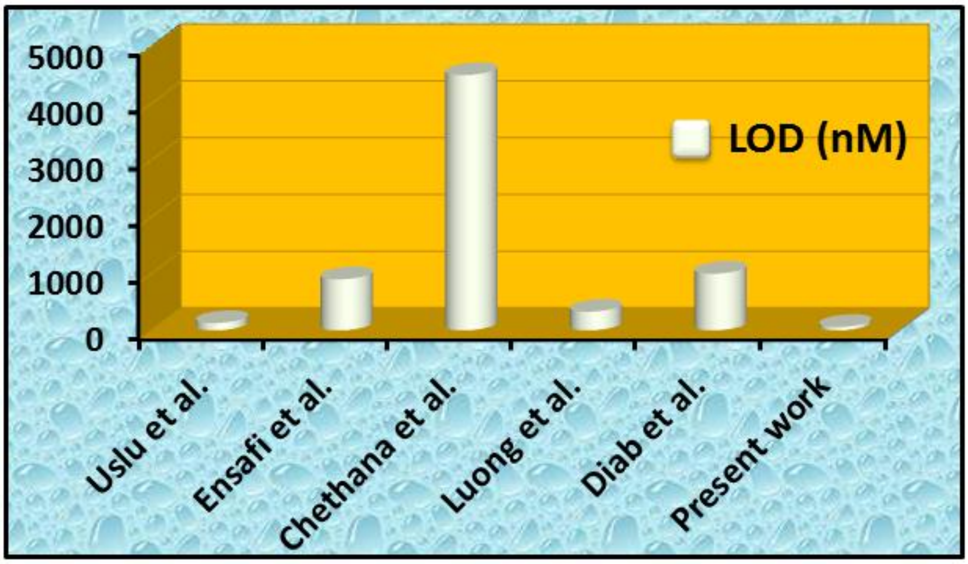

Figure 4.20 The analytical superiority of the present work.

4.4 Conclusions

In conclusion, we have developed a versatile approach to design the nanocrystalline coordination polymer of free standing array having elegant polymeric network with high surface area and extended π–conjugation that allows extensive delocalization over the skeletons, thus enabling efficiently high electron transfer rate. The extended π–conjugated system of fashioned architecture tends to interact with an analyte in a flat–lying geometry, thus facilitate the analyte to approach easily at the molecular periphery and engaging in the hydrogen bonding, hydrophobic and electrostatic interactions. Provided the analyte retain their mobility at the electrode without obstructing the electrode surface by the functional groups of the analytes. This approach is first time successfully extended for an efficient electrochemical detection of CFX in aqueous media using a noncommercial fabricated electrode and has great advantages in the view point of cost, sensitivity, low detection range and facile fabrication. The rapid electron transfer through the nano crystals plays crucial role for the generation of characteristic anodic events. It has illustrated from the experimental data that the precise use of AMT–Ag is imperative for producing the definite current pattern in the signature events. With the encouraging preliminary results, the method is further approved to detect CFX in the clinical formulation (eye drop) and in the biological fluid. These results are highly significant for the sensing of pharmaceutical drugs with variable concentrations of CFX. By modulating the interplay between organic ligand and metal, it will be possible to design NCCPs and nanocrystalline duplexes for a broad spectrum of sensing approaches, which can virtually turn into a widely acceptable device for the sensitive detection of drug candidates. The structural diversity and flexibility of NCCPs will open new windows for research in the fields of nanotechnology and coordination polymers, which significantly expands the landscape of electrochemical sensing.